Reconsidering the Mechanism of Polyglutamine Peptide Aggregation†

Christine C. Lee,‡ Robert H. Walters, and Regina M. Murphy*

Department of Chemical and Biological Engineering, University of Wisconsin, Madison, Wisconsin 53706

Received April 27, 2007; Revised Manuscript Received July 24, 2007

ABSTRACT: There are at least nine neurodegenerative diseases associated with proteins that contain an unusually expanded polyglutamine domain, the best known of which is Huntington's disease. In all of these diseases, the mutant protein aggregates into neuronal inclusions; it is generally, although not universally, believed that protein aggregation is an underlying cause of the observed neuronal degeneration. In an effort to examine the role of polyglutamine in facilitating protein aggregation, investigators have used synthetic polyglutamine peptides as model systems. Analysis of kinetic data led to the conclusions that aggregation follows a simple nucleation−elongation mechanism characterized by a significant lag time, during which the peptide is monomeric, and that the nucleus is a monomer in a thermodynamically unfavorable conformation [Chen, S. M., et al. (2002) *Proc. Natl. Acad. Sci. U.S.A. 99*, 11884−11889]. We re-examined this hypothesis by measuring the aggregation kinetics of the polyglutamine peptide $K_2Q_{23}K_2$, using sedimentation, static and dynamic light scattering, and size exclusion chromatography. Our data show that during the lag time in sedimentation kinetics, there is substantial organization of the peptide into soluble linear aggregates. These aggregates have no regular secondary structure as measured by circular dichroism but have particle dimensions and morphologies similar to those of mature insoluble aggregates. The soluble aggregates constitute approximately 30% of the total peptide mass, form rapidly, and continue to grow over a period of hours to days, eventually precipitating. Once insoluble aggregates form, loss of monomer from the solution phase continues. Our data support an assembly mechanism for polyglutamine peptide more complex than that previously proposed.

Nine CAG repeat diseases are known, of which Huntington's disease is the most common. In all nine diseases, a mutant protein with an elongated polyglutamine (polyQ) region is expressed (*1*). These late-onset neurodegenerative disorders are invariably associated with neuronal inclusions that contain aggregates of the polyQ protein and/or its proteolytic fragments (*2*, *3*). These aggregates are typically fibrillar in nature and are associated with degenerating neurons. Generally, a polyQ region exceeding ∼35−45 repeats leads to the development of the disease phenotype; longer polyQ regions correlate with an earlier age of onset and a greater severity of symptoms (*2*, *4*). The affected proteins have no homology to each other outside of the polyQ region (*2*), differing in size, sequence, and location of the polyQ tract (*2*, *4*).

Several lines of evidence link aggregation of proteins containing expanded polyQ regions with cellular toxicity. For example, delivery of synthetic polyQ aggregates to the nucleus via a nuclear localization sequence caused cell death (*5*). Overexpression of chaperone proteins rescued neurons from polyQ-mediated death in cellular and animal models (*6*−*8*), and small molecules that alter polyQ aggregation in vitro also prevented degeneration in cellular and animal models (*9*−*12*). These and other data suggest a causal connection between polyQ aggregation and neuronal death, motivating research into the role of polyQ in causing protein aggregation.

Synthetic peptides have served as useful model systems for detailed investigation of polyQ aggregation (*13*−*17*). At present, there is no firm consensus about the appropriate structural model. Relying primarily on X-ray diffraction data, Perutz originally suggested a "polar zipper" model for aggregates of $D_2Q_{15}K_2$ but later reanalyzed the data and concluded that the aggregates were water-filled nanotubes, with 20 residues per turn and side chains pointing alternately into and out of the cylinder (*13*, *18*). Interestingly, spontaneous formation of annular aggregates was observed in one computational study of polyQ aggregation (*19*, *20*). Molecular dynamics simulations indicate that such a water-filled tube is energetically unstable and would collapse into a triangular β-helical structure with flat single β-sheet segments linked by planar bends (*21*, *22*). The structural model of a collapsed β-helix has been challenged. Sikorski and Atkins concluded that the most likely structure consists of antiparallel β-sheets, with unusually tight intersheet compaction due to side chain−side chain hydrogen bonding (*23*). Independent X-ray diffraction studies of peptides containing 8−45 glutamines concluded similarly that the peptides aggregated into β-sheet slabs, with the longer peptides folding via multiple reverse turns (*24*).

† Funding was provided by National Science Foundation Grant BES-0330537.

* To whom correspondence should be addressed. Telephone: (608) 262-1587. Fax: (608) 262-5434. E-mail: regina@engr.wisc.edu.

‡ Current address: Merck, Sharp & Dohme, Rahway, NJ.

[1] Abbreviations: BCA, bicinchoninic assay; CD, circular dichroism; DLS, dynamic light scattering; HFIP, hexafluoroisopropanol; HPLC, high-pressure liquid chromatography; PBS(A), phosphate-buffered saline (with azide); SLS, static light scattering; TEM, transmission electron microscopy; TFA, trifluoroacetic acid; ThT, thioflavin T.

10.1021/bi700806c CCC: $37.00
Published on Web 10/11/2007

Wetzel and co-workers pioneered studies of the kinetics of aggregation of polyQ peptides. Using multiple experimental techniques, including thioflavin T (ThT)[1] fluorescence and centrifugation followed by HPLC mass determination to measure aggregate concentration, they observed a classic nucleation−elongation pattern of lag, growth, and plateau in aggregate formation, with aggregation rates increasing with both peptide length and concentration (*15*−*17*). Fitting the kinetic data to a simple mathematical model, the researchers concluded that polyQ peptide aggregation is initiated by the energetically unfavorable conformational conversion of a random coil peptide to a monomeric nucleus (*17*, *25*). Briefly, it was postulated that an unstructured monomer M is in equilibrium with a conformationally distinct monomer M*:

$$M \leftrightarrow M^*$$

described by an equilibrium constant $K_n = [M^*]/[M]$, where $K_n \ll 1$. M* was postulated to serve as a nucleus for formation of fibrils F via irreversible addition of M; growth of F was then assumed to occur by further addition of M:

$$M^* + M \rightarrow F$$

$$F + M \rightarrow F$$

where the rates of both elongation reactions are characterized by a single rate constant, k_e. This model has informed, for example, recent theoretical efforts aimed at describing the conformational ensemble of polyQ monomers (*26*) and the connection between aggregation and cellular toxicity (*27*).

The objective of the current work was to answer the question of whether there are soluble oligomers present during the putative lag phase. The peptide chosen for study was $K_2Q_{23}K_2$, because peptides of the sequence $K_2Q_nK_2$ were used in the other studies (*16*, *17*, *25*) and because preliminary experiments indicated that 23 glutamines were sufficient for fibril formation at moderate concentrations (∼20 μM) and temperatures (37 °C), and at physiological pH and ionic strength. Using laser light scattering and size exclusion chromatography, we show that during the putative lag period the polyQ peptide is not homogeneously monomeric but rather assembles into large soluble linear aggregates that eventually mature into insoluble aggregates. Our results indicate that polyQ peptide aggregation follows an assembly pathway more complex than previously thought.

MATERIALS AND METHODS

Peptide Synthesis and Purification. $K_2Q_7K_2$, $K_2Q_{15}K_2$, and $K_2Q_{23}K_2$ (described subsequently as Q7, Q15, and Q23, respectively) were synthesized using standard Fmoc solid phase methods on a PerSeptive Biosystems Pioneer synthesizer. Lysine flanking residues were added to the polyQ core to increase solubility. Glutamines with a trityl side chain protecting group and lysines with a Boc side chain protecting group were purchased from Novabiochem. The resin used was Fmoc-L-Lys(*t*Boc)-PEG-PS from Applied Biosystems. Resin sites were partially blocked with alanine-Boc to reduce the extent of on-bead aggregation. Extended cycles and double couplings were used to improve yield. After cleavage from the resin and removal of protecting groups with trifluoroacetic acid (TFA), the peptide was precipitated into cold *tert*-butylmethyl ether. Crude peptide was solubilized in a 1:1 solution of water and 2-propanol before being purified by reverse phase HPLC on a Vydac C18 column. Peptide was eluted from the column with a linear gradient of acetonitrile and water with 0.1% TFA, and the peak corresponding to the correct sequence was collected and lyophilized. Purified peptides were determined to have molecular masses of 1427.3 Da (Q7, 1427.7 Da theoretical), 2452.2 Da (Q15, 2452.8 Da theoretical), and 3478.1 Da (Q23, 3477.9 Da theoretical) by MALDI-TOF mass spectrometry.

Sample Preparation. Lyophilized Q23 was disaggregated using a protocol similar to that developed by others (*28*). Briefly, peptide was incubated for 0.5−4 h in a 1:1 solution of TFA and HFIP. After solvent evaporation under a gentle stream of N_2, the peptide was immediately dissolved in water that had been adjusted to pH 3 with TFA. The peptide concentration of the stock solution was typically ∼260 μM. The stock solution was filtered through a 0.45 μm filter, aliquoted, snap-frozen in dry ice and ethanol, and stored at −80 °C.

We found that, although the filtered stock solution was aggregation-free prior to storage, freezing and thawing caused peptide aggregation (data not shown), consistent with previous reports (*17*). Therefore, just prior to each experiment, a vial was thawed and centrifuged at 19 500 rcf for 30 min at 4 °C, and then the supernatant (top 90%) was removed and used immediately. To initiate aggregation, the supernatant was diluted into phosphate-buffered saline (PBSA) [10 mM phosphate, 0.12 M NaCl, and 0.02% (w/v) sodium azide (pH 7.4] to ∼5, 15, or 25 μM. Actual peptide concentrations were determined at the end of each experiment by a BCA (Pierce, Rockford, IL) assay, with ubiquitin as the concentration standard. The concentration of ubiquitin was determined independently by its absorbance at 280 nm, using an extinction coefficient of 0.1495 M^{-1} cm^{-1} (*29*).

Transmission Electron Microscopy (TEM). Samples of Q23 in PBSA were incubated for 4 h or 2 days at 37 °C. A drop of sample was applied to a pioloform-coated grid and stained with methylamine tungstate stain and then imaged with a Philips CM120 scanning transmission electron microscope.

Circular Dichroism (CD). The stock solution was diluted into water at pH 3 to a final peptide concentration of ∼20 μM, and CD spectra were collected in the far-UV range on an Aviv 202SF spectropolarimeter using a 1 mm cell. Spectra were also collected for a peptide sample prepared in 10 mM phosphate and 120 mM NaF (pH 7.4) and incubated at 37 °C.

Sedimentation Assay. Supernatant from the stock solution, prepared as described above, was diluted into PBSA to a final peptide concentration of ∼20 μM and aliquoted into sample tubes containing 40 μL each; the tubes were incubated at 37 °C. At regular time intervals, a sample tube was withdrawn and the contents were diluted further with PBSA to a total volume of 100 μL and then centrifuged at 14 000 rpm for 30 min. The supernatant (top 90%) was carefully removed, and the peptide concentration was determined in triplicate with a BCA (Pierce) assay in the microplate format, using a BioTek EL 800 Universal Microplate Reader. The manufacturer's procedure was followed, except the incubation time was increased from 30 to 90 min and the absorbance was read at 570 nm rather than

at 562 nm. All concentrations are reported as a percentage of the concentration of an uncentrifuged aliquot.

Laser Light Scattering. Samples were prepared from peptide stock solutions diluted into double-filtered (0.22 μm filters) PBSA and then immediately filtered again through a 0.45 μm filter directly into a clean light scattering cuvette. Preliminary experiments showed that there was no loss of material upon filtration (not shown). The cuvette was placed in a 37 °C bath of the index-matching solvent decahydronaphthalene. Dynamic light scattering (DLS) data were collected using a Malvern 4700c system and a Coherent Innova 90C argon ion laser operating at a wavelength of 488 nm. The autocorrelation function at a 90° scattering angle was measured repeatedly over several hours. The apparent *z*-averaged diffusivity $\langle D\rangle_z$ was determined from the autocorrelation function by the method of cumulants. R_{hz}, the apparent *z*-averaged hydrodynamic radius, was calculated from $\langle D\rangle_z$ using the Stokes equation (*30*). On the same samples and at the same time points, the total intensity of scattered light at 90°, $I_s(90°)$, was measured. Scattering from solvent $I_b(90°)$ was subtracted from $I_s(90°)$, and the result was normalized to the scattered intensity of toluene, to adjust for changes in laser power or aperture.

At regular time intervals between 0 and 6 h, the intensity of scattered light as a function of detection angle θ was measured between 20° and 135°. Scattering from buffer alone and toluene was measured at the same angles, and the Rayleigh ratio [$R_s(q)$] was calculated from the scattering data as described previously (*30*). Because preliminary analysis indicated that the particles were very large, the data were graphed as Berry plots, $\sqrt{Kc/R_s(q)}$ versus q^2, where $q = 4\pi n \sin(\theta/2)$, K is an instrument constant (*30*), and c is the mass concentration (grams per cubic centimeter) of the peptide (Supporting Information). The weight-averaged molecular weight, $\langle M\rangle_w$, was determined from the *y*-intercept as described previously (*31*).

Morphological information and the characteristic dimension of the aggregates were extracted by graphing scattering data as a Kratky plot [$q^2R_s(q)Kc = q^2\langle M\rangle_w P(q)$ versus q, where $P(q)$ is the particle shape factor and depends on particle morphology and dimension]. Examination of the data in a Kratky plot reveals information about particle morphology. For example, the plotted data increase monotonically for rodlike particles but increase and then plateau for semiflexible linear chains (*31*); branched semiflexible chains are characterized by curves in which a clear maximum exists before decreasing to a plateau that has a *y*-axis value greater than zero (*32*, *33*), whereas compact globular shapes are indicated by curves with a clear maximum that approach zero at large q values (*31*). Given the shape of the curves on the Kratky format (see Results), we chose to fit the data to model equations for $P(q)$ describing a semiflexible "star" (a particle with a central point from which emanates semiflexible linear arms):

$$P(q) = \frac{1}{fL_{c,a}^{\ 2}}[2(2-f)\int_0^{L_{c,a}}(L_{c,a}-t)\phi\,dt + (f-1)\int_0^{2L_{c,a}}(2L_{c,a}-t)\phi\,dt] \quad (1)$$

where the function $\phi = \phi(\tau,\lambda_\kappa,\theta)$ is described elsewhere (*30*). The unknown parameters in eq 1 are the number of branches (f), the contour length of an arm ($L_{c,a}$), and the Kuhn statistical segment length (l_k), which is a measure of stiffness. For a linear chain, $f = 2$ and eq 1 reduces to $P(q)$ of a semiflexible chain (*34*). These parameters were determined by fitting data to the equations using the parameter estimation program Athena. We neglected polydispersity in this analysis; thus, our calculations of average size and shape should be considered as approximate. To confirm our choice of model for particle morphology, we attempted to fit the data to equations for $P(q)$ to other morphologies (specifically, hard spheres and soft spheres), none of which were able to recapitulate the data (not shown).

From the fitted values of f, $L_{c,a}$, and l_k, we calculated the radius of gyration R_g:

$$R_g^{\ 2} = \frac{l_k^{\ 2}}{4f}\left[(3f-2)\left(\frac{2L_{c,a}}{3l_k}\right) - f + \frac{l_k}{L_{c,a}} - \frac{(2-f)}{2}(1 - e^{-2l_k/L_{c,a}})\left(\frac{l_k}{L_{c,a}}\right)^2 - (f-1)(1-e^{-l_k/L_{c,a}})\left(\frac{l_k}{2L_{c,a}}\right)^2\right] \quad (2)$$

We calculated an independent estimate of the hydrodynamic radius of an equivalent sphere, R_h, from numerical integration of the particle shape factor (*31*, *32*):

$$R_h = \frac{\pi}{2}[\int_0^\infty P(q^2)\,dq]^{-1} \quad (3)$$

Size Exclusion Chromatography. Samples were prepared as described and incubated at 37 °C. Aliquots were removed at regular time intervals over several days and analyzed by size exclusion chromatography (SEC) on a Superdex 75 PC 3.2/30 column (Pharmacia), which has a molecular mass range of 3−70 kDa, using a Waters 625LC system. The mobile phase [PBS (pH 7.4) with 10 mM phosphate and 120 mM NaCl] flow rate was set to 0.05 mL/min; an overfilled 50 μL sample loop was used to apply a calibrated volume of sample, and peaks were detected by absorbance at 220 nm. The column was calibrated using bovine serum albumin, ovalbumin, β-lactoglobulin, ribonuclease A, ubiquitin, and insulin B chain. We have previously observed that peptide aggregates may be lost, by trapping and/or adsorption to the column and/or filter (*35*). Therefore, to account for this possibility, we injected identical samples into the same instrument but without the column in place and obtained a total peak area. The weight fraction of a species eluting from the column at a specific elution time was determined by dividing the area of that peak by the total area of the sample injected without the column in place.

RESULTS

Selection of Polyglutamine Peptide Length and Sample Preparation Conditions. In preliminary experiments, we prepared Q7, Q15, and Q23 at 15−25 μM at different pH values (pH 3, 7.4, or 12 with 10 mM buffer) and salt concentrations (0, 0.15, 0.4, and 2 M NaCl). All peptides initially dissolved completely. Samples were incubated for 2 weeks at 37 °C and then analyzed for aggregation by ThT staining and by filtration through a 0.45 μm filter. At pH 7.4 and 0.12 M NaCl, we observed no ThT signal and no loss of material upon filtration for the Q7 sample, a positive ThT signal but little loss of material (<5%) for Q15, and a

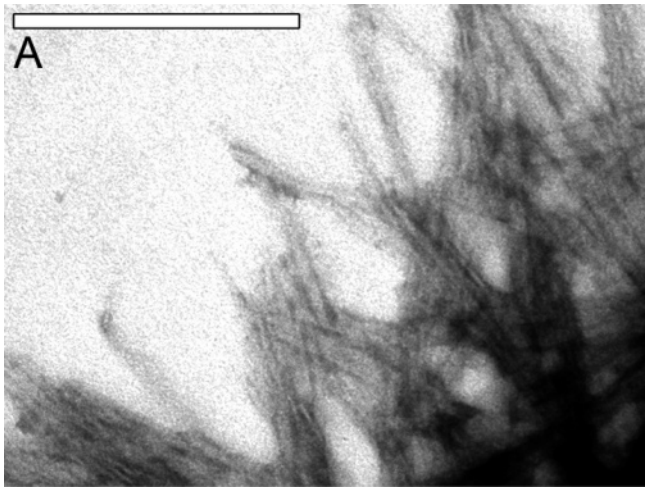

FIGURE 1: TEM image of Q23 aggregates. Q23 samples were prepared at ~15−20 μM in PBSA and then incubated at 37 °C for 2 days prior to imaging. The samples were not rigorously disaggregated prior to preparation. Images are representative of a large number of fields examined. The length of the white bar is 200 nm.

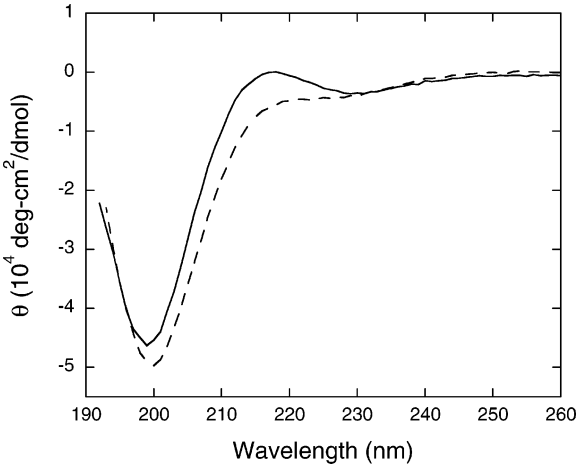

FIGURE 2: CD spectra of Q23 at acidic and neutral pH. A stock solution of disaggregated and frozen Q23 was thawed and centrifuged. Supernatant was removed and diluted to 20 μM in water adjusted to pH 3 with TFA, and CD spectra were recorded immediately (—). In the other process, supernatant was diluted to 20 μM in 10 mM phosphate/120 mM NaF buffer (pH 7.4) and incubated for 2 days at 37 °C prior to the spectra being recorded (− − −). Spectra taken 1 h after dilution were identical (not shown). Background spectra on the appropriate buffer was subtracted.

positive ThT signal and substantial loss of material (~60−70%) for Q23. Q23 aggregates were imaged by electron microscopy (Figure 1). We observed thin linear aggregates (~5−6 nm across), ribbonlike assemblies of aligned linear aggregates, and bundles of fibrils and/or ribbons. These images are qualitatively consistent with other published TEM observations (*17*). From these preliminary experiments, we confirmed that Q23 assembles into structured fibril-like aggregates. We chose Q23 for further detailed study due to its initial solubility and its ability to aggregate over time.

We next established conditions under which Q23 is monomeric and disordered. HPLC-purified peptide was lyophilized, dissolved in HFIP and TFA, dried under nitrogen, redissolved in water at pH 3, filtered, snap-frozen, and stored at −80 °C. After thawing and being centrifuged, supernatant was removed and diluted to 20 μM at pH 3. The solution was analyzed by size exclusion chromatography. A single peak eluted at 35.3 min, corresponding to a molecular mass of 3.4 kDa (3.5 kDa expected) on the basis of column calibration (Supporting Information). The peak area was 0.99 AU/min, while the area of a replicate peptide sample injected without the column in place was 1.01 ± 0.09 AU/min. Since there was quantitatively complete recovery of the injected peptide in the monomer peak, we concluded that the peptide in the prepared stock solution was fully monomer, within experimental error. To further test this conclusion, we examined the peptide in the stock solution by laser light scattering, a technique that is highly sensitive to the presence of aggregates that might escape detection by a mass-based assay such as size exclusion chromatography. The intensity of scattered light from prepared samples of Q23 at 6 and 55 μM in water at pH 3 was measured. At 6 μM, $I_s(90°) = 2.9$ kcps (thousand counts per second), and $I_s(90°) - I_b(90°) = 0.3$ kcps. At 55 μM (10-fold higher concentration), $I_s(90°) - I_b(90°) = 2.8$ kcps, a ~10-fold increase. For solutions of small particles, the excess scattering intensity is a linear function of total mass concentration c and molecular weight M_w. $I_s - I_b \propto cM_w$. The proportional increase in scattering with concentration indicates that M_w does not change, consistent with a nonaggregating sample. Scattering was too weak to obtain accurate measures of M_w or to collect autocorrelation curves and determine R_{hz}. These data gave no evidence for aggregates in this sample, despite the use of a technique that is highly sensitive to aggregates. Finally, to look for evidence of secondary structure, Q23 in water at pH 3 was examined by circular dichroism. CD spectra indicated that the peptide was predominantly disordered (Figure 2). The small positive band at 218 nm has been interpreted by others as evidence of minor polyproline II helical structure in polyglutamine peptides (*36*). Taken together, these data establish that Q23 is appropriate for further study of the kinetics of aggregation of polyglutamine peptides because (a) an initially disordered and monomeric state can be established (at pH 3, no salt) and (b) over time, at physiological pH and salt and at 37 °C, fibril-like aggregates appear.

Kinetics of Aggregation. Q23 was diluted from stock (water at pH 3) into phosphate buffer [10 mM phosphate and 120 mM NaF (pH 7.4)] to a final concentration of ~20 μM and incubated at 37 °C, to initiate aggregation. CD spectra were collected 1 h (not shown) or 2 days (Figure 2) after dilution. The spectra show that Q23 lacks regular secondary structure and remains disordered under these conditions. The small decrease in ellipticity centered at 218 nm as the solution changed (from pH 3 without salt to pH 7.4 with salt) may indicate a subtle conformational shift and a loss of the minor polyproline II structural element.

Similarly prepared solutions were distributed into aliquots and incubated at 37 °C. Tubes were regularly sampled over several days, then their contents were centrifuged and analyzed for the concentration of soluble (supernatant) peptide (Figure 3A). There was an apparent lag time of >75 h before measurable sedimentation was observed. Beyond that point, aggregation continued slowly over several days. This is consistent with previous reports that polyQ peptides with lengths ranging from 20 to 32 glutamines had lag times of roughly 25−100 h under similar conditions and that rates of aggregation are slow (*15*). We analyzed the data assuming

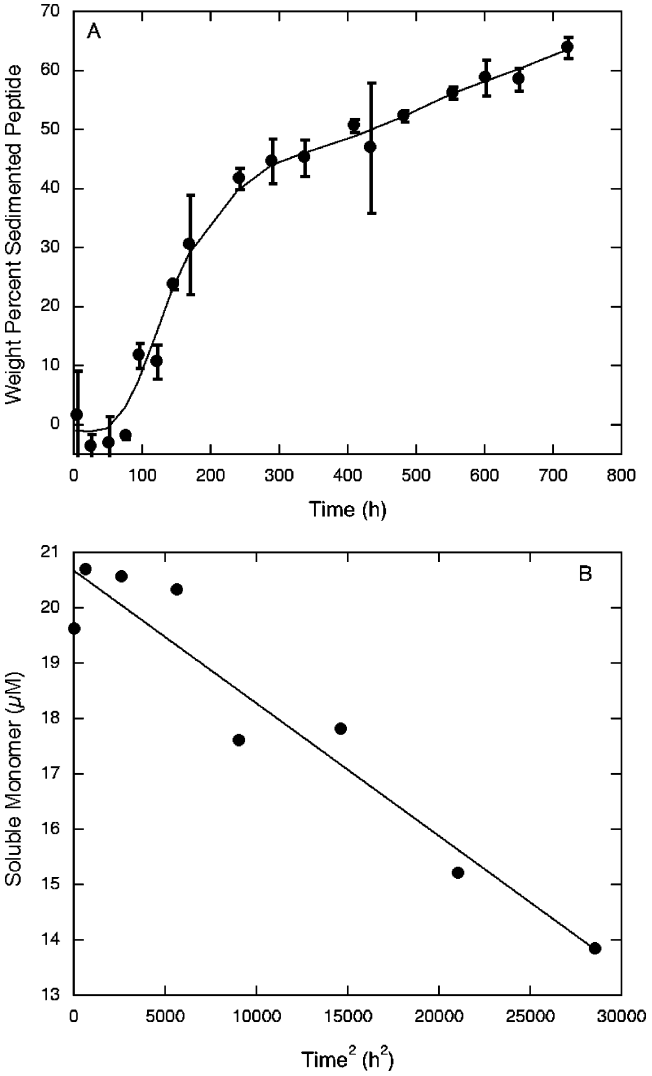

FIGURE 3: Sedimentation kinetics of Q23. Q23 was rigorously disaggregated as described, then diluted to ~20 μM in PBSA, aliquoted into tubes, and incubated at 37 °C. At the indicated times, a tube was centrifuged, and the peptide concentration in the supernatant was determined. (A) The weight percent peptide sedimented, calculated from the ratio of the supernatant concentration to the total concentration in an uncentrifuged sample. Error bars indicate the standard deviation of three replicate concentration measurements. (B) Supernatant peptide concentration, expressed as monomer, at early times (≤30% aggregated material). The concentration is plotted vs t^2. The solid line is the linear regression fit of the data to eq 4.

the nucleation−elongation model with a monomeric nucleus (*16*):

$$-\frac{d[M]}{dt} = k_e K_n [M]^2 + k_e [M][F]$$

$$\frac{d[F]}{dt} = k_e K_n [M]^2$$

with initial conditions where $[M] = [M]_0$ and $[F] = 0$ at $t = 0$. Following the approach of Chen et al. (*16*), we applied the simplifying approximations that $[M] \sim [M]_0$ at small conversion (small t) and that $K_n[M] \ll [F]$ (equivalent to assuming that monomer loss via association with M* is small compared to monomer loss via association with F), one derives

$$[M] = [M]_0 - \frac{1}{2} k_e^2 K_n [M]_o^3 t^2 \quad (4)$$

The data up to 30% aggregation were plotted versus t^2, and a linear relationship was observed (Figure 3B). Equation 4 was fit to the data by nonlinear regression, and an estimate for $k_e^2 K_n$ of 0.004 M^{-2} s^{-2} was obtained. This is similar to values obtained by others (*16*) for Q28, Q36, and Q47 (0.001, 0.09, and 1.8 M^{-2} s^{-2}, respectively).

This analysis of the sedimentation data implicitly assumes that all soluble peptide is monomeric. To test this assumption, laser light scattering data were collected on samples of Q23 diluted from a pH 3 stock into PBSA and held at 37 °C. Both the total scattered intensity at 90° and the apparent hydrodynamic radius were measured. Representative data from samples at 5, 15, and 22.5 μM are shown in Figure 4. If the peptide remained monomeric upon dilution, we should have observed scattering intensities of ~1−2 Kcps and an R_{hz} of ~1−2 nm (if an adequate signal-to-noise ratio could have been obtained). Instead, the scattering intensities measured shortly after placing the cuvette in the sample holder were clearly above background. As shown in Figure 4, total scattered intensity continued to increase over time, with the rate of increase strongly dependent on the concentration. Importantly, no lag time was detectable at any concentration. Similarly, the earliest measurements of R_{hz} demonstrate the presence of particles that are substantially larger than monomer. R_{hz} continued to grow over several hours in a concentration-dependent manner, with no evidence of a lag time.

After several hours, a decrease in $I_s(90°)$ and a decrease in the quality of the R_{hz} measurement indicated incipient precipitation. The onset of precipitation was delayed as the concentration decreased: precipitates were evident at approximately 12 h for 22.5 μM and 17 h for 15 μM. Precipitation was not observed during the 20 h experimental time for the sample at 5.3 μM. Laser light scattering is extremely sensitive to aggregates; incipient precipitation can be detected by this technique when the quantity of precipitate is too small to be detected by mass-based assays (e.g., sedimentation).

To distinguish between monomer and soluble oligomers, samples prepared in a manner identical to that for the samples used for light scattering analysis were analyzed by size exclusion chromatography. Samples were analyzed immediately, 2, 4, 6, and 24 h after preparation, and then randomly from 3 days to up to 4 weeks. A single peak eluted at the expected time for monomers (data not shown). However, the peak area of the monomer was smaller than that of a replicate sample injected without the column in place. (The precision of these experiments is low, due to the relatively weak absorbance of the samples and the errors in accurate determination of the baseline.) In contrast, at pH 3 and in the absence of salt, complete recovery of the injected peptide in the monomer peak was obtained, as described earlier. The weight fraction of monomer (w_{mon}) was calculated as the ratio of the peak area of the monomer to the peak area of the entire sample without the column. As shown in Figure 5, w_{mon} equaled 0.72 ± 0.1 (mean ± range) initially for Q23 in PBSA, remained constant for over 24 h, and then decreased slowly over a period of several days to weeks. The transition from constant w_{mon} to decreasing w_{mon} occurred

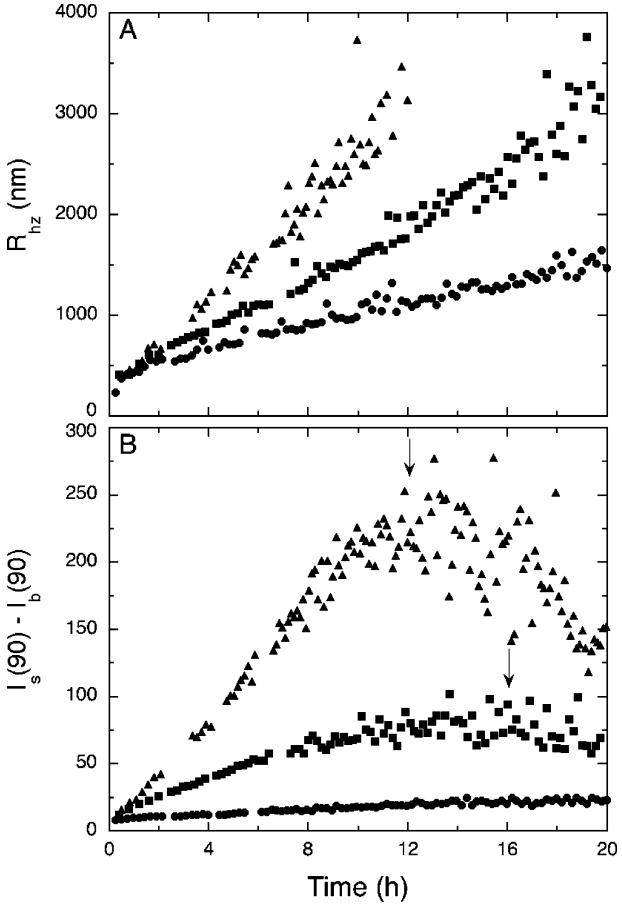

FIGURE 4: Kinetics of aggregation of Q23. Disaggregated peptide was diluted to 5 (●), 15 (■), or 22.5 μM (▲) in PBSA, then immediately filtered, and placed in a cuvette at 37 °C. (A) Apparent *z*-averaged hydrodynamic radius (R_{hz}), as determined from cumulants analysis of autocorrelation data collected at a scattering angle of 90°. (B) Total intensity of scattered light at 90°. Scattering due to the solvent was subtracted. Arrows indicate incipient precipitation.

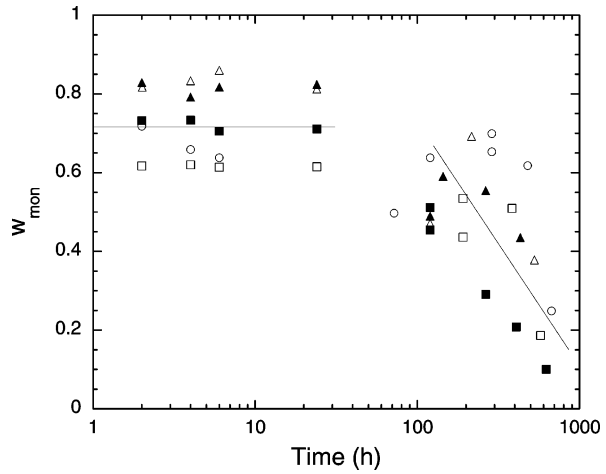

FIGURE 5: Change in monomer mass fraction of Q23 with time. Disaggregated peptide was diluted to 8 (○), 16 (■ and □), or 22−23 μM (▲ and △) in PBSA and then incubated at 37 °C. Aliquots were removed at the indicated times and analyzed by size exclusion chromatography. Weight fraction monomer w_{mon} was calculated as the ratio of the area of the peak eluting as a monomer divided by the total peak area of the same sample injected without the column in place. Lines are drawn as an aid to the eye.

in the same time frame as the end of the lag time as detected by sedimentation (Figure 2). Q23 was prepared at ~20 μM

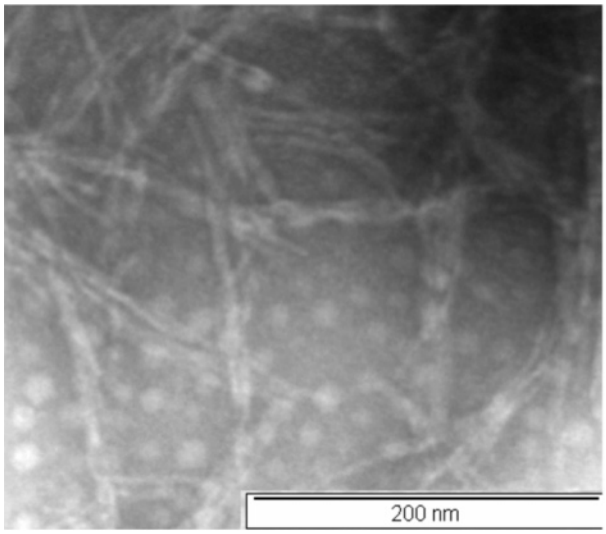

FIGURE 6: TEM image of early aggregates of Q23. Q23 was rigorously disaggregated, then diluted into PBSA at ~20 μM, and incubated for 4 h prior to imaging. Images are representative of a large number of fields examined.

and examined 4 h after preparation by TEM. Long thin aggregates are clearly observed (Figure 6), although the aggregates are less dense and less numerous than those in an aged sample (Figure 1).

Taken together, these data demonstrate that Q23 is initially fully soluble but eventually forms precipitatable aggregates under physiological conditions, with a lag time of >75 h at ~20 μM as measured by sedimentation. During this lag time, Q23 lacks regular secondary structural elements and remains disordered. However, only ~70% of the soluble peptide is monomeric. Laser light scattering and TEM confirm that large soluble aggregates with a linear morphology are present during the putative lag time.

Aggregate Size and Morphology. TEM images indicated that the soluble Q23 oligomers were generally long and thin (Figure 6). To further examine the size and shape of these oligomers, multiangle static light scattering (SLS) data were collected on Q23 in PBSA at three different concentrations (6.5, 18, and 22.5 μM), between 0 and 6 h after sample preparation. The data were plotted in the Berry format to extract $\langle M \rangle_w$ (Supporting Information). Results at 2, 4, and 6 h are summarized in Table 1. $\langle M \rangle_w$ increased with an increase in concentration and increased over time, with the greatest rate of increase at the highest concentration. The data were replotted in the Kratky format (Figure 7) to extract additional information about the shape and characteristic dimensions of the aggregates. The shapes of the curves are indicative of semiflexible linear (Figure 7A) or branched (Figure 7B,C) particles. The data were fit to eq 1, the model equation for $P(q)$ of a semiflexible linear chain ($f = 2$) or semiflexible star ($f > 2$). The fitted curves are plotted beside the data, and the parameters are summarized in Table 1.

We further analyzed the results by combining the data in Table 1, additional light scattering data collected at intermediate time points (not shown), and the size exclusion data in Figure 5. The weight fraction of aggregated peptide (w_{agg}) was calculated as $1 - w_{mon}$, where w_{mon} is taken from Figure 5 and is ~0.7. The average molecular mass of the aggregates (M_{agg}) was estimated as $\langle M \rangle_w / w_{agg}$, and the average linear

Table 1: Size of Q23 Aggregates, As Determined by Analysis of Multiangle Static Light Scattering Data[a]

concentration (μM)	time (h)	$\langle M \rangle_w$ ($\times$1000 kDa)	f	$L_{c,a}$ (nm)	l_k (nm)	R_g (nm)	R_h (nm)
6.5	2	2.3 $\pm$ 0.2	2	900 $\pm$ 200	140 $\pm$ 40	190 $\pm$ 40	132
	4	2.9 $\pm$ 0.2	2	820 $\pm$ 80	170 $\pm$ 20	200 $\pm$ 20	135
	6	2.6 $\pm$ 0.1	2	700 $\pm$ 100	140 $\pm$ 30	170 $\pm$ 20	117
17.8	2	13.4 $\pm$ 0.1	2.9 $\pm$ 0.3	1100 $\pm$ 300	130 $\pm$ 30	220 $\pm$ 50	165
	4	18.9 $\pm$ 0.1	3.2 $\pm$ 0.3	1000 $\pm$ 200	120 $\pm$ 30	220 $\pm$ 40	164
	6	24.1 $\pm$ 0.2	3 $\pm$ 3	1000 $\pm$ 2000	80 $\pm$ 100	200 $\pm$ 300	159
22.5	2	47.4 $\pm$ 0.4	4.5 $\pm$ 0.4	1300 $\pm$ 200	150 $\pm$ 20	280 $\pm$ 40	220
	4	69.2 $\pm$ 0.7	4.7 $\pm$ 0.8	1400 $\pm$ 400	120 $\pm$ 40	260 $\pm$ 70	206
	6	126 $\pm$ 1	7 $\pm$ 2	1600 $\pm$ 700	100 $\pm$ 50	300 $\pm$ 100	213

[a] Multiangle static light scattering data shown in Figure 5 were fit to eq 1 to determine the number of branches (f), the length of each arm ($L_{c,a}$), and the Kuhn length (l_k). For the sample at 6.5 μM, the number of branches (f) was set equal to 2. Mean $\pm$ 90% confidence interval is reported. The radius of gyration (R_g) and the hydrodynamic radius (R_h) were then calculated from the particle size parameters per eqs 2 and 3.

density (ρ_{lin}) was calculated from $M_{agg}/(fL_{c,a})$ (*35*). Results of these calculations are summarized in Figure 8, which shows the concentration-dependent change in the size and shape of Q23 aggregates over time.

Several trends are evident from the data in Table 1 and Figure 8. First, at the lowest concentration, Q23 assembled rapidly into long, semiflexible chains ($\sim$1.5 μm long, with $\rho_{lin} \sim$ 6 kDa/nm); these aggregates grew only slightly over several hours. At the intermediate concentration, linear aggregates of similar length appear that grow slowly by branching, as indicated by the increase in f, and by thickening, as indicated by the increase in ρ_{lin} from 10 to 18 kDa/nm. Similarly, at the highest concentration, aggregate growth occurs primarily by branching and thickening, with a greater number of branches, and a higher linear density (up to 43 kDa/nm), than at the lower concentrations. Assuming a solid cylindrical geometry for the arms (*35*), we estimate that these linear densities correspond to diameters of $\sim$4 nm (6 kDa/nm) to $\sim$10 nm (43 kDa/nm). These estimates are consistent with TEM images and typical in general of fibrillar aggregates. The mass of peptide in the soluble aggregates remains constant at $\sim$30% of total peptide during the lag phase. Thus, the slow growth of these soluble aggregates during the lag phase is primarily attributable to entanglement and lateral alignment of preexisting oligomers, and not to further incorporation of monomer into the soluble aggregates.

R_g and R_h were calculated from the fitted parameters using eqs 2 and 3; results are included in Table 1. The calculated R_h (determined from SLS) was significantly smaller than the apparent R_{hz} measured by DLS (Figure 4). Complications can arise in analysis of DLS data because the autocorrelation function may include diffusion modes other than center-of-mass translation, such as rotational diffusion of anisotropic particles, segmental diffusion if particles are flexible, correlated motion in the event of long-range particle−particle interactions, or hindered diffusion in semidilute solutions. We further analyzed the DLS data using CONTIN, a method that allows for analysis of multimodal distributions. We observed that CONTIN analysis repeatedly indicated the presence of two diffusing populations, a faster-diffusing (smaller size) population that was on the same order of magnitude as R_h calculated from the SLS data and a slower-diffusing (larger size) population that was on the same order of magnitude as R_{hz} determined from cumulants analysis of DLS data (not shown). We attributed the faster-diffusing population to isolated aggregates and the slower-diffusing population (large apparent R_{hz}) to dynamic clustering and/or hindered diffusion of the aggregates. Similar behavior has been observed in other aggregating systems (*33*).

DISCUSSION

Synthetic polyQ peptides are useful model systems for investigating glutamine-mediated aggregation mechanisms. Such studies are needed to understand the role of expanded glutamine domains in aggregation of huntingtin, ataxins, and other proteins associated with the trinucleotide expansion diseases. Wetzel and colleagues pioneered the study of the kinetics of polyQ peptides (*15*−*17*, *25*, *28*). Four methods were used to establish the existence of a lag time: ThT fluorescence, 90° scattering in a spectrofluorimeter, centrifugation, and circular dichroism. On the basis of their data, they concluded that aggregation proceeded through lag, growth, and plateau phases, and the lag time was lost if "seeds" (pre-aggregated peptide) were added. The data were interpreted to indicate that polyQ aggregated by a mechanism that included an energetically unfavorable monomeric nucleus but did not involve soluble intermediates (*16*, *25*).

In general agreement with the published studies, we obtained evidence of lag, growth, and plateau phases in a sedimentation assay probing Q23 aggregation kinetics (Figure 2). Aggregation followed a t^2 dependence, per eq 4, and the length of the putative lag phase and the rate of growth were similar to those reported previously by others (*15*−*17*). A long lag time is generally taken as evidence that the initial preparation did not contain preformed aggregates (*16*, *17*). We also found that over the course of several days, Q23 formed aggregates that were insoluble, ThT-positive, and of generally fibrillar morphology (Figure 1).

We next examined the secondary structure of soluble Q23. CD spectra at acidic and neutral pH indicated that the peptide is predominantly disordered (Figure 2). Interestingly, a small positive band at 218 nm was observed for Q23 at pH 3 but not at pH 7.4. A similar band was observed by others for Q5 at neutral pH, but not for Q15 (*15*). This band was interpreted as being indicative of polyproline II helical structure in shorter but not longer polyQ peptides (*36*). We speculate that the modest difference we observed in Q23 CD spectra in different solvents is due to a modest change in the conformational ensemble from extended (pH 3, no salt, 25 °C) to more collapsed (PBSA, 37 °C). There is experimental and theoretical support for the notion that polyQ peptides can adopt both extended and collapsed coil conformations. For example, fluorescence correlation spectroscopy data taken of Q15 to Q53 in PBS at nanomolar

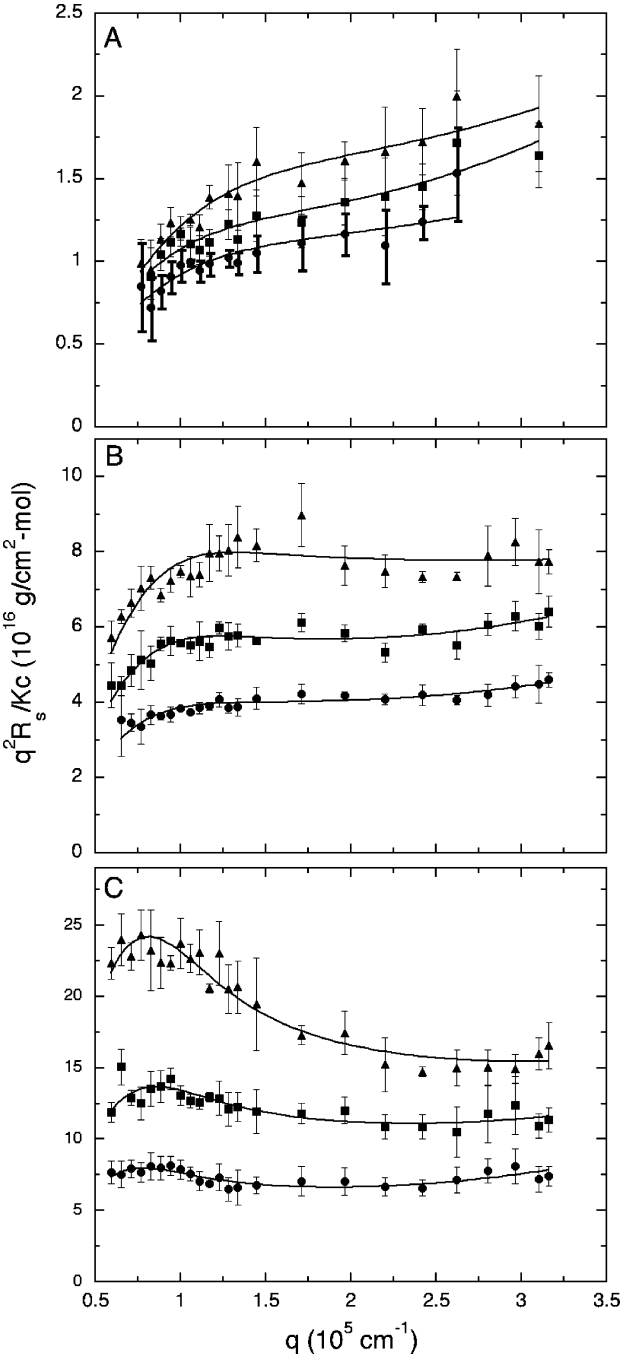

FIGURE 7: Kratky plots of multiangle light scattering of Q23. Total intensity data at multiple scattering angles were analyzed to determine particle shape and dimensions. Data were taken at 2 (●), 4 (■), and 6 h (▲). Lines indicate nonlinear least-squares fits of eq 1 to data: (A) 6.5, (B) 18, and (C) 22.5 μM.

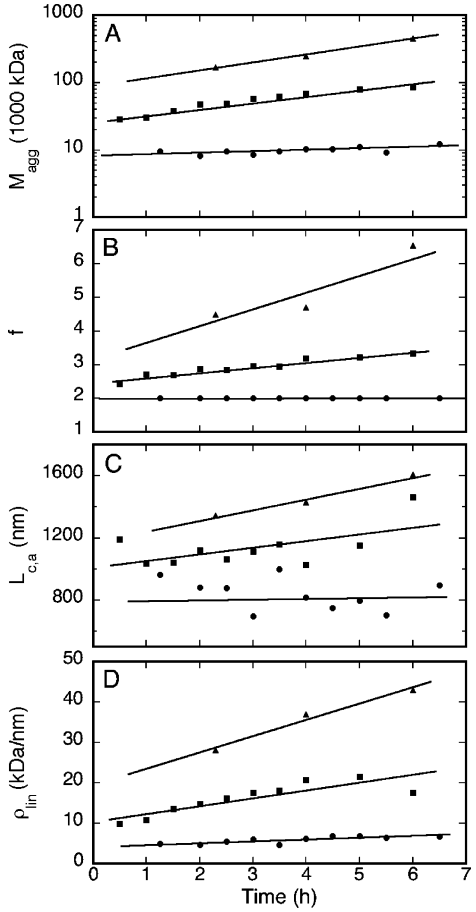

FIGURE 8: Change in aggregate size with time. Values were determined by Kratky analysis of light scattering data, as illustrated in Figure 7. The Q23 concentration was 6.5 (●), 18 (■), or 22.5 μM (▲). (A) Average molecular weight of aggregates, M_{agg}, calculated as $\langle M\rangle_w/(1 - w_{mon})$, where $w_{mon} = 0.72$ from Figure 5. (B) Average number of branches, f, assuming a semiflexible star morphology. For a linear chain, $f = 2$. In analysis of the scattering data at the lowest concentration, f was set equal to 2 and was not a fitted parameter. (C) $L_{c,a}$ is the average length of an "arm". For a linear chain ($f = 2$), the total contour length of the chain equals $2L_{c,a}$. (D) Average linear density $\rho_{lin} = M_{agg}/fL_{c,a}$. ρ_{lin} reflects the average cross-sectional area of the chains.

concentrations (1000-fold more dilute than our experiments) indicated that polyQ monomers are compact and that PBS is a poor solvent (*37*). Molecular dynamics simulations of Q16 monomers suggest that the peptide folds into "collapsed random coils" with a few backbone hydrogen bonds but no regular secondary structure (*20*) and that polyQ monomers populate a restricted conformational ensemble that is heterogeneous and disordered, containing both collapsed and extended conformers, but not a true random coil distribution (*26*).

We next questioned whether there were soluble aggregates, lacking regular secondary structure, present during the putative lag phase. By size exclusion chromatography, dynamic light scattering, static light scattering, and electron microscopy, we clearly detected soluble aggregates during the putative lag phase. Our data demonstrate that a significant (~30%) fraction of the peptide undergoes rapid assembly into large, soluble aggregates. The presence of soluble aggregates is perhaps not surprising, given that PBS is a poor solvent for polyQ peptides (*37*). A comparison to other polymeric systems may be illuminating. Wu and colleagues have reported the existence of soluble aggregates with polymers in poor solvents under dilute conditions. These polymers form collapsed coils; the soluble aggregates are termed "mesoglobules" and are considered as falling between isolated coils and macroscopic precipitation (*38*). Detailed analysis of light scattering data shows that these soluble Q23 aggregates are semiflexible linear assemblies, or moderately branched aggregates of linear assemblies. This conclusion was supported by TEM images indicating the presence of long, thin aggregates during the "lag" phase. The aggregates are very large, containing thousands of monomers on average, and reaching lengths of 1 μm or more. The average

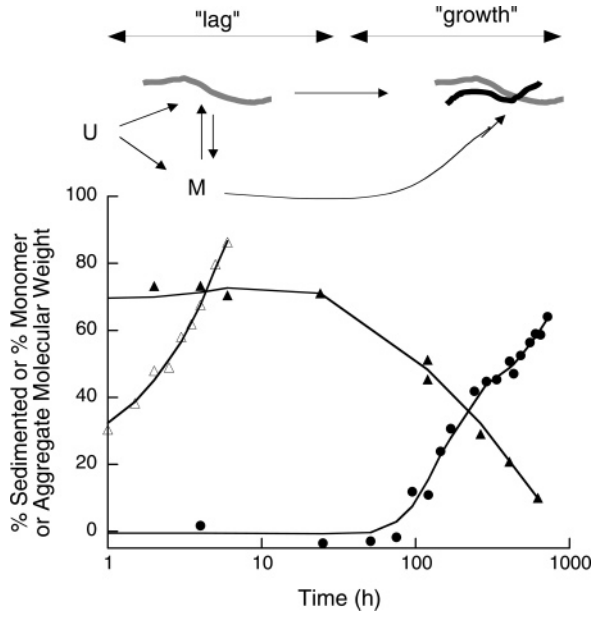

FIGURE 9: Schematic illustrating the proposed kinetic pathway. The data plotted include the percent sedimented from Figure 3 (●), the weight percent monomer from Figure 5 (▲), and the average aggregate molecular weight from Figure 8 (△). Unfolded monomer at pH 3 (U) is diluted into PBSA where it rapidly forms monomer M and soluble linear aggregates (gray). During the lag phase, ~30% of the peptide mass is incorporated into the aggregates, while 70% is monomer (▲). The percent sedimented is zero. Over several hours, these soluble aggregates grow slowly, as indicated by the increase in the average aggregate molecular weight (△). The growth is fueled by coalescence of early aggregates and not by addition of new monomer, since the weight percent monomer does not change during this time. After several hours to a few days, depending on concentration, aggregates begin to precipitate. During the growth phase, the percent sedimented increases while the percent monomer decreases.

molecular weight, the degree of branching, and the rate of growth increased with an increase in concentration.

On the basis of our data, we propose a scheme that is illustrated in Figure 9. At pH 3, Q23 is monomeric and predominantly disordered, but possibly somewhat more extended than a true random coil. Dilution into PBS, a poor solvent for polyglutamine (*37*), along with a temperature increase, initiates a modest shift in the conformational ensemble toward collapsed coils, and a rapid formation of soluble oligomers. During the lag phase, which lasts 3−4 days, Q23 is fully soluble, but only ~70% of the peptides are monomeric (denoted as M in Figure 9). Approximately 30% of the peptide assembles into large oligomers that lack regular secondary structure but are arranged in a linear morphology. This assessment is consistent with CD, TEM, SEC, sedimentation, and light scattering data recorded during the lag phase. Whether there is reversible conversion between M and aggregate (as depicted in Figure 9) remains to be established. The soluble aggregates grow slowly, with the rate of growth increasing with an increase in concentration (Figure 8), but there is no further inclusion of monomer in the soluble aggregates during this phase. Eventually, these aggregates precipitate. Sedimentation could be triggered by slow growth of soluble oligomers until they attain sufficient size to form macroscopic aggregates. Alternatively, strands within the aggregates could undergo conformational rearrangement from disordered to more regular secondary structures. Given that the peptides are pre-assembled, such a conformational transition would likely be highly cooperative. In this scenario, precipitation would be brought on by dehydration and locking in of intermolecular β-sheet hydrogen bonding (*21*).

Once precipitates can be detected by sedimentation, there is a steady increase in the fraction of sedimented material and a decrease in soluble monomer concentration. Monomer loss could be driven by re-establishment of equilibrium between monomer and soluble aggregates, as the soluble aggregates become insoluble and are lost from solution. Alternatively, soluble monomers might directly interact with insoluble aggregates, perhaps by a templated assembly mechanism. This latter possibility is particularly appealing if the onset of the "growth" phase is co-incident with a structural rearrangement in the aggregates from disordered to β-sheet.

In summary, polyglutamine peptides have been postulated to assemble into aggregates via a simple nucleation−elongation mechanism, involving formation of a thermodynamically disfavored monomeric nucleus, and bypassing the formation of soluble intermediates (*16*, *17*, *25*, *27*). However, our data demonstrate that soluble oligomers are indeed formed during the putative lag period and that these oligomers lack a regular β-sheet secondary structure. Similarly, in early work with the Alzheimer's related peptide β-amyloid (Aβ), it was proposed that aggregation followed a nucleation−elongation model, with a lag time prior to aggregation during which the peptide was monomeric (*39*, *40*). Further studies by several groups (*33*, *41*−*45*) clearly demonstrated the existence of soluble aggregates during the putative lag phase, requiring re-evaluation of the mechanism of aggregation. Soluble oligomers have similarly been reported with other fibrillogenic proteins and peptides, including insulin, prion proteins, α-synuclein, and proteins containing expanded polyglutamine domains (*46*−*56*). These aggregates vary in size and shape; aggregates with an elongated morphology but lacking a well-defined secondary structure are sometimes called "protofibrils". Whether soluble oligomers are a direct intermediate to structured fibrils, an off-pathway byproduct, or an intermediate toward amorphous aggregates remains a controversial issue in the amyloidogenesis field (*46*, *50*, *51*, *57*). For Q23, soluble oligomers display particle morphologies and dimensions characteristic of mature fibrillar aggregates, suggesting that they are more likely to be direct precursors of mature fibrils rather than byproducts. Our data support an assembly mechanism for polyglutamine peptide more complex than that previously proposed, but one that is in keeping with phenomena observed with other systems.

ACKNOWLEDGMENT

We gratefully acknowledge the technical assistance of Dr. Gary Case, Dr. Randall Massey, and Dr. Darrell McCaslin.

SUPPORTING INFORMATION AVAILABLE

Representative chromatograms illustrating the method for determining the monomer fraction (Figure S1) and representative Berry plots for determing $\langle M \rangle_w$ (Figure S2). This material is available free of charge via the Internet at http://pubs.acs.org.

REFERENCES

1. Bates, G. (2003) Huntingtin aggregation and toxicity in Huntington's disease, *Lancet 361*, 1642−1644.
2. Orr, H. T. (2001) Beyond the Qs in the polyglutamine disease, *Genes Dev. 15*, 925−932.
3. Wanker, E. E. (2000) Protein aggregation and pathogenesis of Huntington's disease: Mechanisms and correlations, *Biol. Chem. 381*, 937−942.
4. Gusella, J. F., and MacDonald, M. E. (2000) Molecular genetics: Unmasking polyglutamine triggers in neurodegenerative disease, *Nat. Rev. Neurosci. 1*, 109−115.
5. Yang, W., Dunlap, J. R., Andrews, R. B., and Wetzel, R. (2002) Aggregated polyglutamine peptides delivered to nuclei are toxic to mammalian cells, *Hum. Mol. Genet. 11*, 2905−2917.
6. Jana, N. R., Tanaka, M., Wang, G. H., and Nukina, N. (2000) Polyglutamine length-dependent interaction of Hsp40 and Hsp70 family chaperones with truncated N-terminal huntingtin: Their role in suppression of aggregation and cellular toxicity, *Hum. Mol. Genet. 9*, 2009−2018.
7. Satyal, S. H., Schmidt, E., Kitagawa, K., Sondheimer, N., Lindquist, S., Kramer, J. M., and Morimoto, R. I. (2000) Polyglutamine aggregates alter protein folding homeostasis in *Caenorhabditis elegans*, *Proc. Natl. Acad. Sci. U.S.A. 97*, 5750−5755.
8. Carmichael, J., Chatellier, J., Woolfson, A., Milstein, C., Fersht, A. R., and Rubinsztein, D. C. (2000) Bacterial and yeast chaperones reduce both aggregate formation and cell death in mammalian cell models of Huntington's disease, *Proc. Natl. Acad. Sci. U.S.A. 97*, 9701−9705.
9. Zhang, X. Q., Smith, D. L., Merlin, A. B., Engemann, S., Russel, D. E., Roark, M., Washington, S. L., Maxwell, M. M., Marsh, J. L., Thompson, L. M., Wanker, E. E., Young, A. B., Housman, D. E., Bates, G. P., Sherman, M. Y., and Kasantsev, A. G. (2005) A potent small molecule inhibits polyglutamine aggregation in Huntington's disease neurons and suppresses neurodegeneration in vivo, *Proc. Natl. Acad. Sci. U.S.A. 102*, 892−897.
10. Tanaka, M., Machida, Y., Niu, S. Y., Ikeda, T., Jana, N. R., Doi, H., Kurosawa, M., Nekooki, M., and Nukina, N. (2004) Trehalose alleviates polyglutamine-mediated pathology in a mouse model of Huntington disease, *Nat. Med. 10*, 148−154.
11. Sanchez, I., Mahlke, C., and Yuan, J. Y. (2003) Pivotal role of oligomerization in expanded polyglutamine neurodegenerative disorders, *Nature 421*, 373−379.
12. Bodner, R. A., Outeiro, T. F., Altmann, S., Maxwell, M. M., Cho, S. H., Hyman, B. T., McLean, P. J., Young, A. B., Housman, D. E., and Kasantsev, A. G. (2006) Pharmacological promotion of inclusion formation: A therapeutic approach for Huntington's and Parkinson's diseases, *Proc. Natl. Acad. Sci. U.S.A. 103*, 4246−4251.
13. Perutz, M. F., Johnson, T., Suzuki, M., and Finch, J. T. (1994) Glutamine repeats as polar zippers: Their possible role in inherited neurodegenerative diseases, *Proc. Natl. Acad. Sci. U.S.A. 91*, 5355−5358.
14. Sharma, D., Sharma, S., Pasha, S., and Brahmachari, S. K. (1999) Peptide models for inherited neurodegenerative disorders: Conformation and aggregation properties of long polyglutamine peptides with and without interruptions, *FEBS Lett. 456*, 181−185.
15. Chen, S., Berthelier, V., Yang, W., and Wetzel, R. (2001) Polyglutamine aggregation behavior in vitro supports a recruitment mechanism of cytotoxicity, *J. Mol. Biol. 311*, 173−182.
16. Chen, S. M., Ferrone, F. A., and Wetzel, R. (2002) Huntington's disease age-of-onset linked to polyglutamine aggregation nucleation, *Proc. Natl. Acad. Sci. U.S.A. 99*, 11884−11889.
17. Chen, S. M., Berthelier, V., Hamilton, J. B., O'Nuallain, B., and Wetzel, R. (2002) Amyloid-like features of polyglutamine aggregates and their assembly kinetics, *Biochemistry 41*, 7391−7399.
18. Perutz, M. F., Finch, J. T., Berriman, J., and Lesk, A. (2002) Amyloid fibers are water-filled nanotubes, *Proc. Natl. Acad. Sci. U.S.A. 99*, 5591−5595.
19. Marchut, A. J., and Hall, C. K. (2006) Spontaneous formation of annular structures observed in molecular dynamics simulations of polyglutamine peptides, *Comp. Biol. Chem. 30*, 215−218.
20. Marchut, A. J., and Hall, C. K. (2006) Side-chain interactions determine amyloid formation by model polyglutamine peptides in molecular dynamics simulations, *Biophys. J. 90*, 4574−4584.
21. Zanuy, D., Gunasekaran, K., Lesk, A. M., and Nussinov, R. (2006) Computational study of the fibril organization of polyglutamine repeats reveals a common motif identified in β-helices, *J. Mol. Biol. 358*, 330−345.
22. Khare, S. D., Ding, F., Gwanmesia, K. N., and Dokholyan, N. V. (2005) Molecular origin of polyglutamine aggregation in neurodegenerative disease, *PloS Comput. Biol. 1*, 231−235.
23. Sikorski, P., and Atkins, E. (2005) New model for crystalline polyglutamine assemblies and their connection with amyloid fibrils, *Biomacromolecules 6*, 425−432.
24. Sharma, D., Shinchuk, L. M., Inouye, H., Wetzel, R., and Kirschner, D. A. (2005) Polyglutmaine homopolymers having 8−45 residues form slablike β-crystallite assemblies, *Proteins: Struct., Funct., Bioinf. 61*, 398−411.
25. Bhattacharya, A. M., Thakur, A. K., and Wetzel, R. (2005) Polyglutamine aggregation nucleation: Thermodynamics of a highly unfavorable protein folding reaction, *Proc. Natl. Acad. Sci. U.S.A. 102*, 15400−15405.
26. Wang, L. X., Vitalis, A., Wyczalkowski, M. A., and Pappu, R. V. (2006) Characterizing the conformational ensemble of monomeric polyglutamine, *Proteins: Struct., Funct., Bioinf. 63*, 297−311.
27. Colby, D. W., Cassady, J. P., Lin, G. C., Ingram, V. M., and Wittrup, K. D. (2006) Stochastic kinetics of intracellular huntingtin aggregate formation, *Nat. Chem. Biol. 2*, 319−323.
28. Chen, S. M., and Wetzel, R. (2001) Solubilization and disaggregation of polyglutamine peptides, *Protein Sci. 10*, 887−891.
29. Gill, S. C., and von Hippel, P. H. (1989) Calculation of protein extinction coefficients from amino acid sequence data, *Anal. Biochem. 182*, 319−326.
30. Shen, C.-L., Fitzgerald, M. C., and Murphy, R. M. (1994) Effect of acid predissolution on fibril size and fibril flexibility of synthetic β-amyloid peptide, *Biophys. J. 67*, 1238−1246.
31. Burchard, W. (1983) Static and dynamic light scattering from branched polymers and biopolymers, *Adv. Polym. Sci. 48*, 1−213.
32. Huber, K., and Burchard, W. (1989) Scattering behavior of wormlike star, *Macromolecules 22*, 3332−3336.
33. Shen, C.-L., and Murphy, R. M. (1995) Solvent effects on self-assembly of β-amyloid peptide, *Biophys. J. 69*, 640−651.
34. Lowe, T. L., Strzelec, A., Kiessling, L. L., and Murphy, R. M. (2001) Structure-function relationships for inhibitors of β-amyloid toxicity containing the recognition sequence KLVFF, *Biochemistry 40*, 7882−7889.
35. Pallitto, M. M., and Murphy, R. M. (2001) A mathematical model of the kinetics of β-amyloid fibril growth from the denatured state, *Biophys. J. 81*, 1805−1822.
36. Chellgren, B. W., Miller, A.-F., and Creamer, T. P. (2006) Evidence for polyproline II helical structure in short polyglutamine tracts, *J. Mol. Biol. 361*, 362−371.
37. Crick, S. L., Jayaraman, M., Frieden, C., Wetzel, R., and Pappu, R. V. (2006) Fluorescence correlation spectroscopy shows that monomeric polyglutamine molecules from collapsed structures in aqueous solutions, *Proc. Natl. Acad. Sci. U.S.A. 103*, 16764−16769.
38. Chen, H., Zhang, Q., Li, J., Ding, Y., Zhang, G., and Wu, C. (2005) Formation of mesoglobular phase of PNIPAM-g-PEO copolymer with a high PEO content in dilute solutions, *Macromolecules 38*, 8045−8050.
39. Jarrett, J. T., and Lansbury, P. T., Jr. (1993) Seeding one-dimensional crystallization of amyloid: A pathogenic mechanism in Alzheimer's disease and scrapie, *Cell 73*, 1055−1058.
40. Jarrett, J. T., Berger, E. P., and Lansbury, P. T., Jr. (1993) The carboxy terminus of the β amyloid protein is critical for the seeding of amyloid formation: Implications for the pathogenesis of Alzheimer's disease, *Biochemistry 32*, 4693−4697.
41. Harper, J. D., Wong, S. S., Lieber, C. M., and Lansbury, P. T. (1997) Observation of metastable Aβ amyloid protofibrils by atomic force microscopy, *Chem. Biol. 4*, 119−125.
42. Hartley, D. M., Walsh, D. M., Ye, C. P. P., Diehl, T., Vasquez, S., Vassiley, P. M., Teplow, D. B., and Selkoe, D. J. (1999) Protofibrillar intermediates of amyloid β-protein induce acute electrophysiological changes and progressive neurotoxicity in cortical neurons, *J. Neurosci. 19*, 8876−8884.
43. Huang, T. H. J., Yang, D. S., Plaskos, N. P., Go, S., Yip, C. M., Fraser, P. E., and Chakrabartty, A. (2000) Structural studies of soluble oligomers of the Alzheimer β-amyloid peptide, *J. Mol. Biol. 297*, 73−87.
44. Yong, W., Lomakin, A., Kirkitadze, M. D., Teplow, D. B., Chen, S. H., and Benedek, G. B. (2002) Structure determination of micelle-like intermediates in amyloid β-protein fibril assembly

by using small angle neutron scattering, *Proc. Natl. Acad. Sci. U.S.A. 99*, 150−154.
45. Harper, J. D., Wong, S. S., Lieber, C. M., and Lansbury, P. T. (1999) Assembly of Aβ amyloid protofibrils: An in vitro model for a possible early event in Alzheimer's disease, *Biochemistry 38*, 8972−8980.
46. Kayed, R., Head, E., Thompson, J. L., Mcintire, T. M., Milton, S. C., Cotman, C. W., and Glabe, C. G. (2003) Common structure of soluble amyloid oligomers implies common mechanism of pathogenesis, *Science 300*, 486−489.
47. Serio, T. R., Cashikar, A. G., Kowal, A. S., Sawicki, G. J., Moslehi, J. J., Serpell, L., Arnsdorf, M. F., and Lindquist, S. L. (2000) Nucleated conformational conversion and the replication of conformational information by a prion determinant, *Science 289*, 1317−1321.
48. Scheibel, T., Bloom, J., and Lindquist, S. L. (2004) The elongation of yeast prion fibers involves separable steps of association and conversion, *Proc. Natl. Acad. Sci. U.S.A. 101*, 2287−2292.
49. Fink, A. L. (2006) The aggregation and fibrillation of α-synuclein, *Acc. Chem. Res. 39*, 628−634.
50. Haass, C., and Selkoe, D. J. (2007) Soluble protein oligomers in neurodegeneration: Lessons from the Alzheimer's amyloid β-peptide, *Nat. Rev. Mol. Cell Biol. 8*, 101−112.
51. Mukai, H., Isagawa, T., Goyama, E., Tanaka, S., Bence, N. F., Tamura, A., Ono, Y., and Kopito, R. R. (2005) Formation of morphologically similar globular aggregates from diverse aggregation-prone proteins in mammalian cells, *Proc. Natl. Acad. Sci. U.S.A. 102*, 10887−10892.
52. Tanaka, M., Machida, Y., Nishikawa, Y., Akagi, T., Hashikawa, T., Fujisawa, T., and Nukina, N. (2003) Expansion of polyglutamine induces the formation of quasi-aggregates in the early stage of protein fibrillization, *J. Biol. Chem. 278*, 34717−34724.
53. Wacker, J. L., Zareie, M. H., Fong, H., Sarikaya, M., and Muchowski, P. J. (2004) Hsp70 and Hsp40 attenuate formation of spherical and annular polyglutamine oligomers by partitioning monomer, *Nat. Struct. Mol. Biol. 11*, 1215−1222.
54. Scherzinger, E., Schwieger, K., Lurz, R., Lehrach, H., and Wanker, E. E. (1999) Self-assembly of polyglutamine-containing huntingtin fragments into amyloid-like fibrils: Implications for Huntington's disease pathology, *Philos. Trans. R. Soc. London, Ser. B 354*, 991−994.
55. Georgalis, Y., Starikov, E. B., Hollenbach, B., Lurz, R., Scherzinger, E., Saenger, W., Lehrach, H., and Wanker, E. E. (1998) Huntingtin aggregation monitored by dynamic light scattering, *Proc. Natl. Acad. Sci. U.S.A. 95*, 6118−6121.
56. Poirier, M. A., Li, H., Macosko, J., Cai, S., Amzel, M., and Ross, C. A. (2002) Huntingtin spheroids and protofibrils as precursors in polyglutamine fibrillization, *J. Biol. Chem. 277*, 41032−41037.
57. Baskakov, I. V., Legname, G., Baldwin, M. A., Prusiner, S. B., and Cohen, F. E. (2002) Pathway complexity of prion protein assembly into amyloid, *J. Biol. Chem. 277*, 21140−21148.

BI700806C